A&A 377, 285–296 (2001)
DOI: 10.1051/0004-6361:20011110

Astronomy & Astrophysics

Echelle spectroscopy of H_2 in the HH 111 jet

C. J. Davis[1], K. W. Hodapp[2], and L. Desroches[1,3]

[1] Joint Astronomy Centre, 660 North A'ohōkū Place, University Park, Hilo, Hawaii 96720, USA
[2] Institute for Astronomy, 640 North A'ohōkū Place, Hilo, Hawaii 96720, USA
e-mail: hodapp@ifa.hawaii.edu
[3] Dept. of Physics, University of Victoria, PO Box 3055 STN CSC, Victoria, BC V8W 3P6, Canada

Received 22 June 2001 / Accepted 3 August 2001

Abstract. Near-Infrared echelle spectra of the Herbig-Haro knots F–P in the western lobe of the HH 111 outflow are presented. 10 adjacent, parallel slit positions were observed so that the kinematics could be mapped across the width of the flow. We find broad ($FWZI \sim 100$ km s^{-1}), two-component H_2 profiles in the knots nearest the source; the profiles converge to a single, intermediate-velocity peak ($V_{\rm LSR} \sim 50$ km s^{-1}) at knot P. The kinematic signature of the HH 111 jet in H_2 is very similar to that seen at optical wavelengths (from both radial and tangential velocity meaurements). In conjunction with published proper-motion (knot/shock pattern speed) measurements, we interpret the data in terms of a simple geometrical bow shock model. The model infers a high pre-shock velocity, of the order of 200–250 km s^{-1}, with H_2 excitation in the extended bow wings in knots L, H and F, though exclusively near the bow head in knot P, with probably C-type shock excitation throughout.

Key words. interstellar medium: jets and outflows – stars: pre-main-sequence – observations – Herbig-Haro objects: HH 111

1. Introduction

The HH 111 jet is notable for being one of the longest and best collimated Herbig-Haro (HH) flows known to date (Reipurth et al. 1997a). It is driven by a low mass protostar ($L_{\rm bol} \sim 25\ L_\odot$) that is part of a double (and possibly even triple) system that is hidden from view at optical wavelengths by a dense circumstellar core (Stapelfeldt & Scoville 1993). Originally found with the *Very Large Array (VLA)*, the source of the outflow has since been detected with the *Hubble Space Telescope (HST)* at near-IR wavelengths (Reipurth et al. 1999).

In the optical the western, blue-shifted lobe of the jet comprises a series of compact bow shocks, best illustrated in the *HST* images of Reipurth et al. (1997b), that are moving towards the distant, more nebulous HH object HH 311; the eastern lobe of the flow, which is largely obscured from view at optical wavelength (though evident in the near-IR), extends towards HH 113. The total extent of the flow so far observed is almost 1°, or 7.7 pc, on the sky (Reipurth et al. 1997a). The flow is thought to lie within 10° of the plane of the sky (Reipurth et al. 1992). It is also associated with a molecular (CO) outflow (Cernicharo & Reipurth 1996), more recently mapped at high resolution, and shown to be conical near the source, by Nagar et al. (1997) and Lee et al. (2000). The HH 111 jet was first mapped in H_2 line emission by Gredel & Reipurth (1993) and Davis et al. (1994).

In this paper we discuss radial velocity measurements derived from high-resolution, near-IR echelle spectroscopy, data which complement published optical and near-IR proper motion studies and high-resolution images, as well as molecular outflow maps. We first consider the overall kinematics of the observed jet section in relation to other published radial and tangential velocity measurements. We then consider each HH knot in detail and compare the profiles observed with a simple yet relatively powerful geometrical bow shock model. Finally, we briefly discuss the H_2 data in relation to the associated molecular (CO) outflow.

2. Observations

Echelle spectra in H_2 1-0S(1) emission ($\lambda_{\rm vac} = 2.1218334$ μm; Bragg et al. 1982) were obtained on 24 December 1999 (UT) at the UK Infrared Telescope (*UKIRT*) using the facility spectrometer CGS 4. The instrument is equipped with a 256×256 pixel InSb array; the

Send offprint requests to: C. J. Davis,
e-mail: c.davis@jach.hawaii.edu

pixel scale is 0.″41 × 0.″90 (0.″41 in the dispersion direction). A 1-pixel-wide slit was used, resulting in a velocity resolution of ∼8 km s^{-1} (although over-sampled spectra were obtained by physically shifting the array by 1/2 pixel, so that two detector positions were observed per resolution element). The instrumental profile in the dispersion direction, measured from Gaussian fits to sky lines, was 11.3 (±1.5) km s^{-1} . Data at ten parallel, adjacent slit positions were obtained, the offset between each slit measuring 0.4″ (equivalent to the slit width). The slits were orientated at a position angle (PA) roughly parallel with the HH 111 jet axis. The CGS4 image rotator was set to 97°, the nominal jet axis PA (e.g. Reipurth et al. 1997b). However, we found a clear discrepancy (of ∼7°) between each slit and the jet axis (noted in Fig. 1 and evident in Fig. 2), which suggests a possible error in the slit angle calibration. All of the knots were in any case included in our 10 slit positions.

Object-sky-sky-object sequences were repeated a number of times at each slit location to build up signal-to-noise, the sky position being 10″ to the north of the jet axis. Each spectral image was bias subtracted and flat-fielded. Sky-subtracted object frames were then co-added into reduced "groups" (one group frame per slit position). Each reduced group spectral image was subsequently wavelength calibrated using the four adjacent OH sky lines that are present in each raw image (Olivia & Origlia 1992; Davis et al. 2001); the first "raw object frame" observed at each slit location (the first frame in each group) was used as a reference frame in each case.

The IRAF tasks used to wavelength calibrate the data (*IDENTIFY, RE-IDENTIFY, FITCOORDS* and *TRANSFORM*), also correct for distortion along the columns in each image (i.e. along arc or sky lines), via a 3rd-order fit in two dimensions. The *relative* velocity calibration across each spectral image, measured from Gaussian fits to sky lines in "velocity-calibrated and distortion-corrected" raw frames, is estimated to be accurate to ≤4 km s^{-1}. Instrument flexure over the duration of the observations could, however, introduce additional uncertainties in the *absolute* velocity calibration, i.e. by shifting the individual frames with respect to the wavelength reference used to calibrate the reduced group spectral image. By comparing the positions of sky lines in a number of raw frames we found that this effect was small; indeed, the narrowness of the H_2 emission features observed at some locations in the final, reduced data (as compared to the instrumental profile width, which is measured from just one frame), confirms this finding. Nevertheless, flexure could still result in an additional broadening of H_2 lines and a shift in the line centre by a few km s^{-1}. We therefore conclude that the overall velocity calibration is accurate to better than 10 km s^{-1}, while perceived velocity shifts between adjacent spectra observed along the same slit will be considerably more accurate, to within 1 km s^{-1}.

A and G-type bright standards were also observed with the same instrument configuration. These indicate that there are no measurable telluric absorption lines in this narrow wavelength regime that might distort the observed profile shapes.

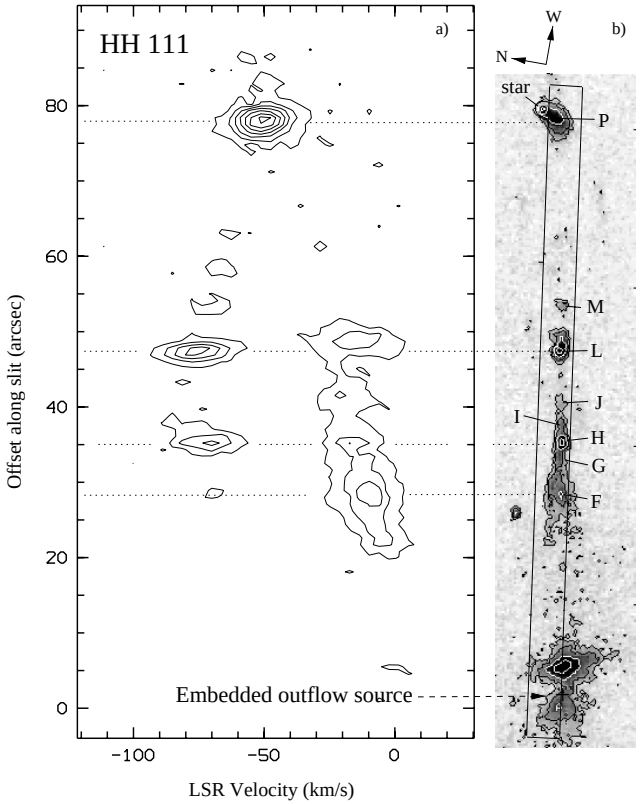

Fig. 1. The spectral image on the left **a)** is the average of all ten spectra (slit positions) observed; it therefore effectively represents the integrated emission from a 4″–wide slit (illustrated in **b)** by the box). For comparison, a narrow-band H_2 2.12 μm (+ continuum) image of the section of the jet observed is presented in b, scaled to the same spatial scale (see Coppin et al. 1998 for details of the image). Some HH knots are labelled. The contours in the P–V plot start at 3× the standard deviation, σ, to the mean background and increase in steps of 4σ. The countours in the H_2 image at right measure 4σ, 8σ (black), 12σ, 16σ... etc. (white).

3. Results

H_2 spectra were obtained at 10 adjacent/parallel slit positions across HH 111. The spacing between slits was 0.4″. Thus, an area 4″ wide (and about 90″ long) was observed. The spectral images from each slit position have been added to give the position-velocity (P–V) plot in Fig. 1. The velocity scale in this plot, and in all subsequent figures, is Local Standard of Rest (LSR); the systemic velocity of the source, derived from (sub)mm observations of the source region in optically-thin CO isotopes, is +8.5 km s^{-1} (Cernicharo & Reipurth 1996). On the narrow-band H_2 image shown in Fig. 1 (adapted from the data of Coppin et al. 1998) we also indicate the section of the blue-shifted HH 111 jet lobe observed.

Strong emission was detected from knots P, L, H and F. The H_2 peak towards knot P in the averaged

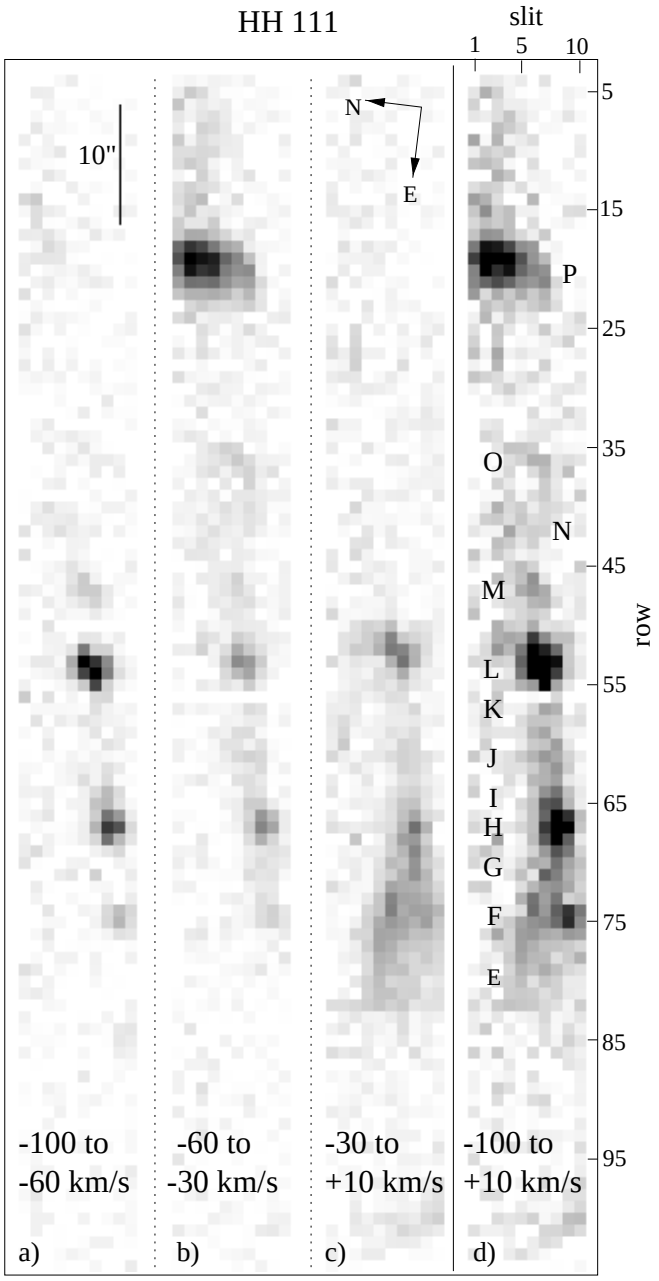

Fig. 2. Channel maps showing the distribution of high **a)**, intermediate **b)**, and low **c)** velocity H_2 emission in HH 111 (LSR velocity ranges are indicated). The right-hand image **d)** is the addition of the other three images and thus represents an image of integrated H_2 in the section of the jet observed. Note that the pixel scale is $0.9''$ (along the slit) by $0.4''$ perpendicular to the slit (the slitwidth). Thus, the aspect ratio of each image is 4:9 (horizontal:vertical) and the scale-bar is only applicable to the vertical axis. The positions of the discrete optical HH knots resolved by *HST* (Reipurth et al. 1997b) are labelled.

spectral image (Fig. 1a) is symmetric and very narrow (full-width half maximum [*FWHM*] ~ 20 km s^{-1}), though it is blue-shifted to $V_{\rm LSR} \sim -50$ km s^{-1}. Nearer the source, the H_2 profiles broaden dramatically; towards knots L and H the full-width zero intensity (*FWZI* – measured between points on the spectrum where the flux reaches the $\sim 2\sigma$ background noise level) of extracted spectra measure $\sim$110 km s^{-1} and $\sim$90 km s^{-1}. These profiles are double-peaked, with no emission detected at intermediate velocities (i.e. at the same velocity as knot P). The profile associated with the fan-shaped HH knot F peaks at only $V_{\rm LSR} \sim -10$ km s^{-1}, though it also extends out to blue-shifted velocities of $\sim$–100 km s^{-1}. Further downwind, between knots L and P, the very faint H_2 emission detected at the $3\sigma-5\sigma$ level indicates a steady "narrowing" of profile widths along the jet axis.

Channel maps constructed from the H_2 echelle data are presented in Fig. 2. In Fig. 2d we also show an "image" of HH 111 constructed from the 10 spectral images (each was collapsed into a 1-D image strip; the 10 columns thus represent the integrated signal from each adjacent slit). The positions of discrete optical knots or bow shocks, resolved by *HST* (Reipurth et al. 1997b) are also marked in Fig. 2d. Here one can clearly see that, at the highest radial velocities, only knots L, H and the compact peak associated with knot F are detected. The more extended "wings" of knot F (which are resolved into a separate broad bow, knot E, in optical *HST* images; Reipurth et al. 1997b) are evident at lower radial velocities (Fig. 2c). Note also that knot P is, again, only detected at intermediate velocities (between -60 km s^{-1} and -30 km s^{-1}; Fig. 2b).

The overall kinematic picture described above is very similar to that derived from high-dispersion optical spectrocopy, obtained at a similar spatial and spectral resolution (though only with a single, $2''$ wide slit; Reipurth et al. 1997b). The optical and near-IR observations exhibit three common properties: 1) the velocity dispersion steadily increases between knot P and the knots closer to the source (knot F and knot E), 2) towards knot P emission lines are single-peaked and blue-shifted to intermediate velocities ($V_{\rm LSR} \sim -50$ km s^{-1} in H_2, [SII] and Hα), while further upwind around F and E the profiles become double-peaked, the peaks straddling the radial velocity seen in knot P, and 3) the broadest profiles are observed towards the bright knot L (where the Hα lines reach almost 200 km s^{-1} *FWZI*; the widths of the H_2 lines will be limited by molecular dissociation).

Figures 1 and 2 illustrate the global velocity structure across HH 111. In Figs. 3–6 we show the line profiles observed across the brightest knots, P, L, H and F, in more detail. Each spectrum, identified by its slit number and row number, corresponds to a given pixel in the image in Fig. 2d.

Beside each spectrum in Figs. 3–6 we mark the peak LSR velocity and *FWHM* line width (in brackets) measured from Gaussian fits to the line. Fits were made to the entire profile in each spectrum (i.e. from the "zero-counts" baseline on either side of the emission line), regardless of any slight asymmetries that might be present. Generally, most lines are in fact "symmetric" and close to Gaussian in shape, so errors from the fitting are rather small, of the order of a few km s^{-1}. As mentioned in Sect. 2, absolute velocity measurements are likely to be accurate to only about 5–10 km s^{-1}. However, errors due to

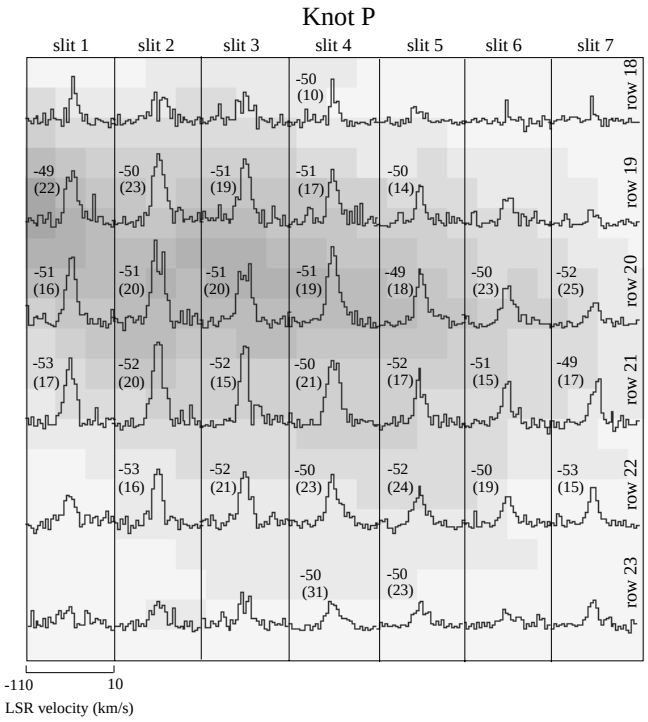

Fig. 3. H_2 profiles across knot P, extracted from 7 adjacent slit positions (see Fig. 2d). Each spectrum covers an area of $0.4'' \times 0.9''$. The spectra are superimposed onto a greyscale image of Knot P. North and east are orientated in the same sense as in Figs. 1 and 2, i.e. (approximately) to the left and downwards respectively. The HH 111 flow direction is upwards in this and all other figures. The numbers next to each spectrum are the mean and *FWHM* from Gaussian fits to each line.

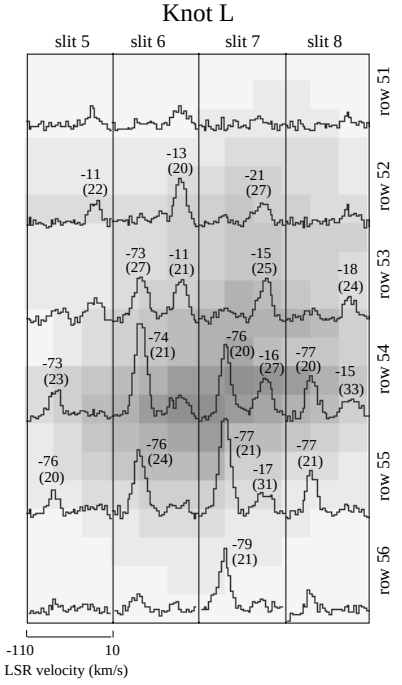

Fig. 4. H_2 profiles across knot L, presented in the same way as for knot P (see Fig. 3 for details). The numbers next to each spectrum are the mean and *FWHM* from Gaussian fits to each line; where two well-separated components are observed, two Gaussian fits were applied.

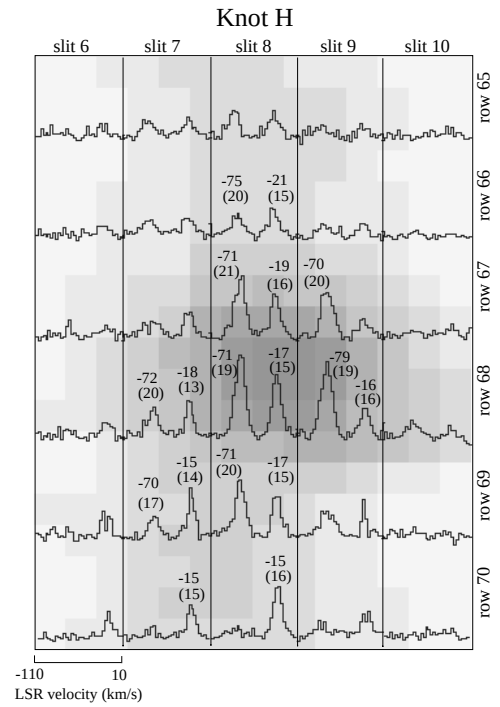

Fig. 5. H_2 profiles across knot H, presented in the same way as for knot P (see Fig. 3 for details). The mean and *FWHM* from Gaussian fits to each component are noted.

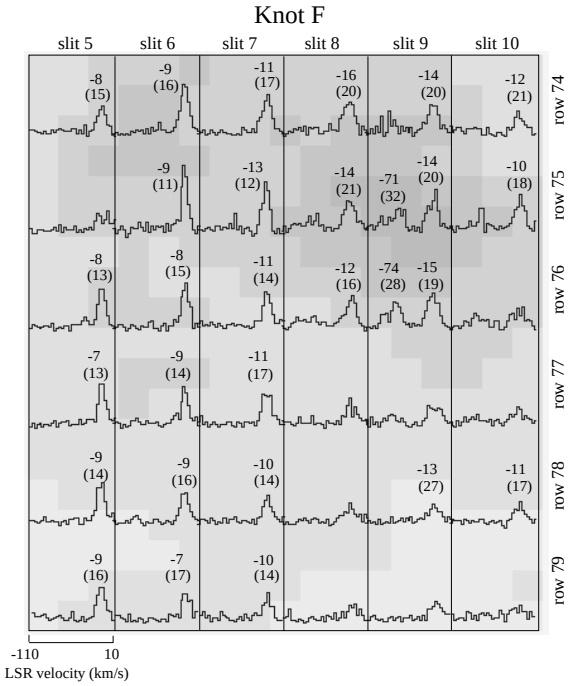

Fig. 6. H_2 profiles across knot F, presented in the same way as for knot P (see Fig. 3 for details). The mean and *FWHM* from Gaussian fits to each component are noted.

distortion of the profiles along the slit are much smaller, and will be negligeable compared to the errors associated with the Gaussian fitting. Thus, any perceived change in peak velocity or *FWHM* between adjacent spectra in Figs. 3–6 is expected to be real. In cases where two

velocity components are clearly present, two Gaussians were fitted to the data and so two sets of measured values are included in the plot.

Below we consider the kinematic properties of each knot separately.

3.1. Knot P

In optical *HST* observations of the jet (Reipurth et al. 1997b) knot P appears as a well-defined, conical (almost triangular) bow shock with a diameter in the bow flanks approaching $\sim 10''$. It is situated a few arseconds to the south-east of an unrelated field star (Fig. 1). The limb-brightened tips of the bow wings are detected in H_2 emission above and below the jet axis (Coppin et al. 1998), although this emission is too far off-axis to be observed in these echelle data.

One might expect the H_2 profile shapes to be dictated by the geometry of the HH 111P bow. The profiles in Fig. 3 are, however, all clearly symmetric and single-peaked, with very little evidence for extended line-wing emission (with the possible exception of spectra in slit 4, rows 22 and 23 which have a weak red-shifted wing). Over much of knot P the profiles are centred at $V_{\rm LSR} \sim -50$ km s^{-1} and are typically 20 km s^{-1} wide *FWHM*. We see no evidence for a change in line width or line peak velocity as we move from the leading edge upwind through the bow shock (i.e. down slit 4 in Fig. 3) or across the width of the bow (from left to right in Fig. 3). Instead, the radial velocity is remarkably constant, given that this extended bow-shaped HH object is spatially resolved in these observations.

3.2. Knots M-L-H

Like knot P, knots L and E (E is merged with knot F in our H_2 image and echelle spectroscopy) appear bow shock shaped in the optical *HST* images of Reipurth et al. (1997), although both are only about $3''$ in diameter. Between L and E there are half-a-dozen other, more compact knots, the brightest in both optical and H_2 emission lines being knot H. All of these knots exhibit curved or bow-shaped morphologies in the *HST* images and so, again, we would expect line-emission profile shapes to be dictated by bow shock geometry.

Across knot L (Fig. 4) we observe radically changing H_2 line profiles. The two velocity components observed across this feature peak at $V_{\rm LSR} \sim -75$ km s^{-1} and ~ -15 km s^{-1}; the components are of the order of 20–30 km s^{-1} wide *FWHM* throughout. Yet the relative intensities of these two components change across knot L, the high-velocity component (*HVC*) becoming stronger relative to the low-velocity component (*LVC*) towards the rear (eastward side) of the emission peak; at the leading edge of knot L (rows 51 and 52 in Fig. 4) the *LVC* clearly dominates. We also find that both components become slightly more blueshifted – by a few km s^{-1} – as we again move eastward (upwind) across the knot. Note that this trend is particularly evident in the *HVC* where the line peaks are strong; the velocity calibration of each spectrum relative to its neighbour along each slit is known to be very good, certainly less than 1 km s^{-1} (see Sect. 2); the accuracy of the Gaussian fitting used to measure the velocities is also high, of the order of 1–2 km s^{-1}. The peak velocity increase in the *HVC* towards the rear of knot L is therefore thought to be real. Indeed, this trend continues downwind and across knot M: the six spectra observed in M (at a 5σ level or higher; not shown here) peak between -69 and -72 km s^{-1}, i.e. they are less blue-shifted than in Knot L. No *LVC* is observed in knot M (Fig. 2).

The spectra from knot H are again double-peaked (Fig. 5). The *HVC* and *LVC* peak velocities are within a few km s^{-1} of $V_{\rm LSR} \sim -71$ km s^{-1} and ~ -18 km s^{-1} respectively; component profile widths are again of the order of 15–20 km s^{-1} (*FWHM*). In knot H the relative intensities of the *LVCs* and *HVC*s change in a similar fashion to those across knot L, although the effect is less dramatic.

3.3. Knot E/F

Low- and high-velocity components are also observed in knot F (Fig. 6), although the *HVC* is weak in relation to the *LVC* and is confined to the emission peak. Knot F is notable for having extended wings that are bright in H_2 emission (see Fig. 1). The line profiles across these wings are consistently very narrow, no wider in fact than the instrumental broadening. Moreover, the line profiles peak at between -8 km s^{-1}and -11 km s^{-1}, increasing to -14 to -16 km s^{-1} near the leading edge (and emission peak) in this knot. Note, however, that the H_2 emission in the region shown in Fig. 6 derives from at least two bow shocks, knot F and the more extended bow knot E (Reipurth et al. 1997b). The narrow, low-velocity component in row 77–79 therefore likely derives from the oblique wings of bow shock E.

4. Discussion

4.1. H_2 excitation in molecular bow shocks

The two velocity components evident in the H_2 observations of knots F to L are relatively unique among protostellar flows. Given sufficient spectral resolution, asymmetric and double-peaked profiles have been detected in the wakes of some molecular bow shocks (e.g. Davis & Smith 1996; Yu et al. 2000; Davis et al. 2000, 2001), although this is not the case for all bow shocks (Davis et al. 1996; Tedds et al. 1999). Double-peaked H_2 profiles should be a natural result of the hollow shell-like morphology of molecular bows, even if the bow is unresolved (e.g. Hartigan et al. 1987; Völker et al. 1999; Tedds et al. 1999), since the near and far sides of the bow shock shell, seen in projection, will deflect material in opposite directions. The difference between the maximum and minimum velocities measured in the wings of the overall profile are then equivalent to the velocity of the bow shock with respect to the pre-shock

medium (Hartigan et al. 1987). In the case of H_2 profiles, the maximum extent of the lines will, however, be limited to roughly twice the dissociation speed limit ($v_{\rm d}$) of H_2 (Smith & Brand 1990; Davis et al. 2000).

J-type bow shocks should not produce extremely wide H_2 profiles, since without ambipolar diffusion and hence magnetic "cushioning" of the approaching shock front H_2 will be dissociated for shock speeds above 20–25 $\rm km\,s^{-1}$ (Kwan 1977; Smith 1994). The full extent of observed profiles should thus be limited to $2v_{\rm d} \sim 50\ \rm km\,s^{-1}$. Only for highly-magnetised C-shocks could $2v_{\rm d}$ exceed 80–100 $\rm km\,s^{-1}$ (Smith & Brand 1990; Smith 1994).

Here we investigate whether a simple, geometrical, bow shock model can explain the overall H_2 profile widths observed in HH 111 as well as the velocity separation between the *LVC*s and *HVC*s in the knots nearest the source. The model is applied specifically to HH 111, although more general results are given in the Appendix. We assume that the two velocity components observed in HH 111 are excited in the near and far sides of a hollow, bow shock shell (illustrated in Fig. 7). The bow moves along the jet axis at speed $v_{\rm bow}$ (measured with respect to the stationary driving source – in this case, VLA 1). The bow and jet are surrounded by a "cocoon" of slow-moving, low-density material. The cocoon is itself bounded by a shell of dense, swept-up gas which separates the cocoon from the ambient medium. The cocoon has presumably been swept out by a bow shock further down-stream, and so the cocoon gas is assumed to be moving parallel with the jet axis at speed $v_{\rm coc}$. Note that numerical bow models do often produce this cocoon plus dense shell scenario (Raga et al. 1995; Völker et al. 1999; Downes & Ray 1999). Moreover, a coaxial, hollow, molecular shell has already been observed around the inner jet section in CO maps of HH 111 (Lee et al. 2000).

In the oblique bow shock wings the angle between the jet axis and the tangent to the shock surface, α, is small. The normal component of the shock velocity, $v_{\rm sn}$ will also be small here. Specifically,

$$v_{\rm sn} = (v_{\rm bow} - v_{\rm coc}){\rm sin}\alpha. \quad (1)$$

The velocity of the post-shock gas ($v_{\rm post}$) at a given position in the bow wings (defined by the angle α) is then given by

$$v_{\rm post}^2 = (v_{\rm sn}{\rm cos}\alpha)^2 + (v_{\rm coc} + v_{\rm sn}{\rm sin}\alpha)^2. \quad (2)$$

The angle of this velocity vector with respect to the jet axis, θ, is given by

$$\theta = \sin^{-1}(v_{\rm sn}{\rm cos}\alpha / v_{\rm post}) \quad (3)$$

and hence, the observed radial component of the velocity of the post-shock gas (along the line of sight) is given by:

$$v_{\rm rad} = v_{\rm post}{\rm cos}(\psi \pm \theta). \quad (4)$$

Here ψ is the inclination angle of the jet axis with respect to the line of sight; in the case of HH 111 this is known to be about 80° (Reipurth et al. 1992). The angle $\theta + \psi$ is specific to emission from the far side of the bow shock surface (the edge furthest from the observer), while $\theta - \psi$ is used for the same position on the near side of the bow surface (the point where the tangent to the shock surface subtends the same angle α with respect to the jet axis).

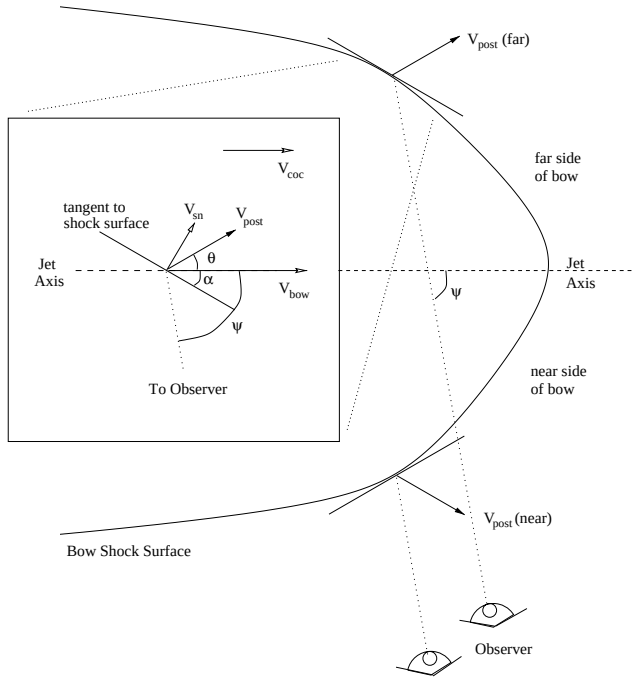

Fig. 7. Schematic diagram of a simple bow-shock model. The diagram in the box is a blow-up of one region on the bow surface, defined by the angle α.

The front and rear sides of the bow shock shell will produce two velocity components and so potentially two line-emission peaks when seen in projection. A range of velocities will contribute to these two components because of the curvature of the two shock surfaces; the observed line components may therefore be quite broad. The highest velocities will occur near the bow head where α is largest. However, for bright (observable) H_2 emission α will be limited to regions in the bow flanks where the shock speed normal to the bow surface does not exceed the H_2 dissociation speed limit, $v_{\rm d}$ (Smith 1994). This maximum angle, $\alpha_{\rm d}$, is given by:

$$\alpha_{\rm d} = \sin^{-1}(v_{\rm d} / [v_{\rm bow} - v_{\rm coc}]) \quad (5)$$

where $v_{\rm d}$ is a speed above which H_2 is destroyed. $v_{\rm d}$ is of course dependent on the "type" of shock observed, in other words, whether J- or C-type (Draine et al. 1983; Draine & McKee 1993). In the extreme case of a low ionisation fraction, a strong magnetic field, and so a high Alfvén speed in the pre-shock gas (a C-type shock), $v_{\rm d} \sim 50\ \rm km\,s^{-1}$; in a J-type shock, $v_{\rm d}$ will be at best half this value (Kwan 1977; Smith 1994).

How, then, does the model compare with our observations of the HH 111 jet? For HH 111 we already know a number of model parameters. We have, from published

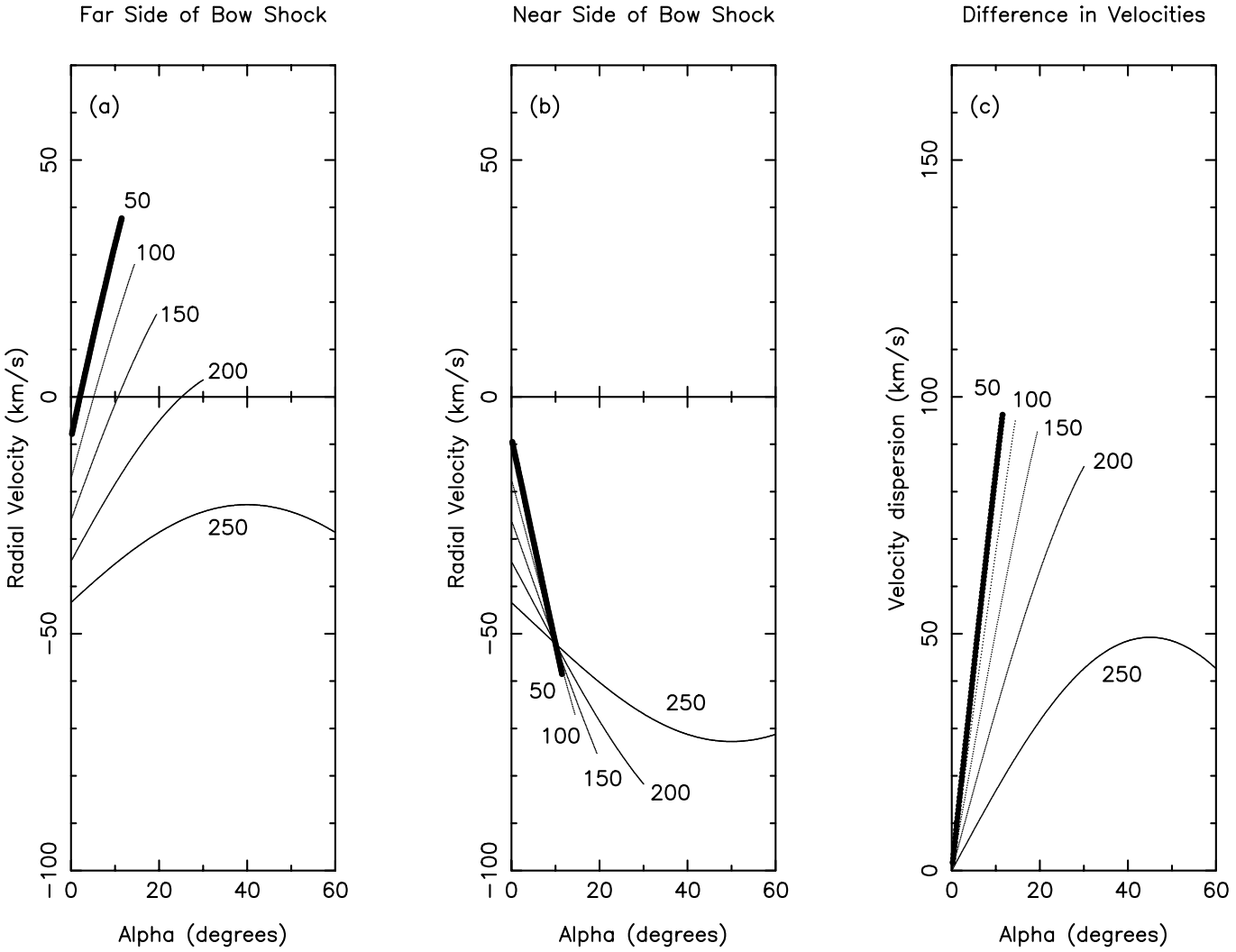

Fig. 8. Plots showing how the observed radial velocity of gas excited in the bow shock wings varies with angle, α (see text for details). Graphs **a)** and **b)** give the radial velocities predicted from gas excited in the near and far sides of the hollow bow shock shell. Positive velocities are red-shifted with respect to the observer, negative velocities blue-shifted. In **c)** we show the resulting velocity dispersion when the near and far sides of the bow are seen in projection. In **a**–**c)** curves for different values of $v_{\rm coc}$ (indicated next to each curve) are plotted. Throughout we adopt a bow shock velocity $v_{\rm bow} = 300$ km s^{-1} and a jet inclination angle of $\psi = 80°$. Note that all velocities in **a)** and **b)** are with respect to the outflow source which in the model is assumed to be stationary with respect to the observer. In HH 111 the LSR velocity of VLA 1 is +8.5 km s^{-1}and so observed radial velocities should be blue-shifted (reduced) by this amount.

optical and near-IR proper motion measurements, a good idea of what $v_{\rm bow}$ is, since tangential LSR velocities of the order of 300 km s^{-1} have been measured (although the uncertainties are high, typically 25–50%; Reipurth et al. 1992; Coppin et al. 1998). We also know the inclination angle of the flow with respect to the line-of-sight, ψ. Since $\psi \sim 80°$, we adopt a "typical" bow shock velocity (along the jet axis with respect to the source which, in our model, is in the rest frame) of $v_{\rm bow} = 300$ km s^{-1}. As mentioned above, the range of values of α for which H_2 is excited into emission is also limited: in the case of a C-shock (with $v_{\rm d} \sim 50$ km s^{-1}), for $v_{\rm coc} \sim 20$ km s^{-1}, $\alpha_{\rm d} \sim 10°$ (Eq. (5)); for faster pre-shock gas, e.g. $v_{\rm coc} = 200$ km s^{-1}, $\alpha_{\rm d} \sim 30°$. We therefore limit our model to values of α less than $\alpha_{\rm d}$, although note that if the difference between $v_{\rm bow}$ and $v_{\rm coc}$ is less than $v_{\rm d}$, H_2 will be excited into emission across the entire bow surface.

We use the model to predict the range of velocities one should observe from the front and rear sides of each bow shock shell in HH 111. The curves in Fig. 8 show how the radial velocity of shocked H_2 varies with angle α; the extent of each curve therefore covers the range of velocities predicted. Separate curves are plotted for different values of $v_{\rm coc}$; $v_{\rm bow}$ is fixed for all curves at 300 km s^{-1}. The range of α plotted applies to the extended bow wings, where α is small; each curve is only drawn between $\alpha = 0$ and $\alpha = \alpha_{\rm d}$, as defined by Eq. (5) for the five values of $v_{\rm coc}$ considered (we assume C-type shock excitation and use

$v_d = 50$ km s^{-1}). We also plot (in Fig. 8c) the *difference* between the radial velocities of the gas in the near and far sides of the bow. This difference is only approximately equal to the observed velocity dispersion, since we assume α is the same for the near and far sides of the bow seen in projection. This will only be the case for large inclination angles (i.e. for a jet near the plane of the sky), or if the bow shock – or the region of the bow where α changes rapidly (near the bow cap) – is unresolved. In either case, the observed velocity dispersion will be dictated by the maximum value of α included in the telescope beam. ψ is known to be $\sim$80° for HH 111, and the bow shocks are observed to be small in optical *HST* images, only a few times larger than our CGS 4 pixels, so the plot in Fig. 8c is probably applicable to our HH 111 spectra. A more accurate plot of observed velocity dispersion would require a more sophisticated model involving a pre-defined bow-shock shape.

At low values of α (in the extended wings of the bow shock) the shock has little effect on the velocity of the cocoon gas and so the observed radial velocities are close to the radial component of the (preshock) cocoon velocity, v_{coc}, for each curve. As α increases (as we approach the bow cap), the near and far sides of the bow increasingly deflect the cocoon gas in opposite directions, thus yielding a higher overall velocity dispersion in Fig. 8c; indeed, near the bow head the value for the velocity dispersion will approach that of the overall bow shock velocity (the difference between the bow and cocoon velocities). As was shown by Hartigan et al. (1987), for an unresolved bow that emits over its entire surface (i.e. where all values of α are observed), the maximum velocity dispersion should be equivalent to the shock velocity. We note here that in Fig. 8c the dispersion values predicted by the model approach the difference between v_{bow} and v_{coc} (the bow shock velocity) for each curve plotted. Lastly, we mention that the curves in Fig. 8b cross at a point where $\alpha + \psi = 90°$. This results from the fact that, for $\alpha > 10°$, the higher shock velocities (lower values of v_{coc}) produce the more blue-shifted gas; for $\alpha < 10°$, the radial velocities approach the velocity of the line-of-sight component of v_{coc}.

The model is of course limited. We do not consider what the minimum values of α and the shock velocity ($v_{bow} - v_{coc}$) are that still induce observable H_2 emission. Nor do we take into account the effects turbulence and/or cooling will have on the dynamics of the shocked H_2; instead, we assume that, at a given position on the bow surface, the post-shock gas is accelerated to the full velocity of the normal component of the shock velocity. Also, we have no knowledge of whether the density of the pre-shock "cocoon" gas is high enough to produce the observed H_2 flux. Furthermore, we ignore the possible contribution of emission from a "reverse shock" or Mack disk.

The model is also strictly two-dimensional. Towards the limb-brightened edges of a real 3-D bow shock the shocked gas is deflected in the plane of the sky, so the radial component of the pre-shock velocity will not change as the gas passes through the shock. One would expect to see narrow, single-peaked profiles along the edges of a bow and only double-peaked lines along the central axis and through the cap of the bow. The curves in Fig. 8 therefore illustrate only the maximum *range* of velocities produced along the jet axis by the near and far sides of the bow shock surface (seen in projection). Here the greatest dispersion of radial velocities will be produced. Indeed, in some cases (see Fig. 8 and also the Appendix) the velocity dispersion described by the curves from the near and far sides of the bow shell will not overlap; then, one would expect to see separate peaks, as we do in HH 111. The fact that we do not see marked changes in profile shapes and velocities across the width of HH 111 is probably a result of the coarse velocity and spatial scales of the echelle observations. Nevertheless, the model does still constrain many of the bow shock parameters in the HH 111 jet.

It is clear from Fig. 8 that because the bows observed along the axis of the HH 111 jet are travelling at high speed (they possess high proper motions), then even in the oblique bow wings where α is low, molecular material can be accelerated to relatively high speeds. The peaks in the two-component profiles observed in HH 111 knots L to F are separated by $\sim$50 km s^{-1}. The observed radial LSR velocities of the *LVC* and *HVC* gas are of the order of -18 ± 5 km s^{-1} and -72 ± 5 km s^{-1} respectively, which translate to $LVC \sim -25$ km s^{-1} and $HVC \sim -80$ km s^{-1} when we take into account the velocity of the system (the VLA1 source) with respect to the observer. These two components are about 30–40 km s^{-1} wide, however, so if the *HVC* and *LVC* derive from the two sides of the same bow, then gas must be accelerated to radial velocities of approximately -5 km s^{-1} to -45 km s^{-1} (the *LVC*) in the far side and -60 km s^{-1} to -100 km s^{-1} (the *HVC*) in the near side. This is possible if the pre-shock gas is fast-moving ($v_{coc} \sim 200-250$ km s^{-1}) and the bulk of the observed H_2 is excited in the section of the bow wings where α lies in the range $10°-30°$ (see Figs. 8a, 8b). A slightly lower value of v_{coc} yields lower values for the *HVC* and *LVC* components, resulting in more widely spaced peaks. And of course if H_2 is excited over more of the bow surface (over a wider range in α), the dispersion of velocities associated with the *HVC* and *LVC* profiles will increase until the discrete components observed in HH 111 merge to form a single, though double-peaked, profile. The *HVC*s and *LVC*s in the HH 111 bows are clearly well-separated (Figs. 4–6); the H_2 emission must therefore be confined to the bow wings. Note also that, because the HH 111 flow axis is inclined towards the observer (blue-shifted), the far side of each bow shock will be seen projected slightly ahead of the near side. The far side produces the low-velocity component (Fig. 8a); the symmetrically-located near side the higher-velocity gas (Fig. 8b). Hence, the *LVC* should extend slightly *ahead* of the *HVC*, precisely as is observed in knot L (Fig. 4), as well as to a lesser extent in knot H (Fig. 5 – down slit 8) and around the emission peak in knot F (Fig. 6 – slits 8 and 9).

The lower-velocity, single-peaked profiles observed in the extended wings of knots F and H may also be accounted for, since here α will remain essentially constant across the region of each bow covered by each spectrum. For $\alpha < 10°$, the emission from the near and far sides of the bow will be accelerated to roughly the same low radial velocities provided, as above, $v_{\rm coc}$ is high ($\sim$200−250 km s^{-1}).

We can also explain the single-peaked profiles observed in knot P, where $V_{\rm LSR}$(peak) ~ -50 km s^{-1} and $FWZI \sim 40$−50 km s^{-1}. We assume the same inclination angle and bow shock velocity as for the other HH knots further upwind. Unlike the single-peaked profiles from the extended wings of knots F and H, however, the H_2 profiles in knot P must predominantly derive from a region near the bow head, since little or no H_2 emission is observed in the bow wings in knot P (Coppin et al. 1998). Our model supports emission from a region near the bow cap if $\alpha > 20°$ (Fig. 8). A slightly higher value of $v_{\rm coc}$ is then needed (higher than used above for the upwind knots) to explain the narrow, blue-shifted H_2 profiles. Indeed, the differential velocity between the bow and pre-shock ambient medium must be low to facilitate the survival of H_2 in the almost "face-on" bow cap. If $v_{\rm coc} \sim 250$ km s^{-1} radial velocities in the range -25 km s^{-1} to -75 km s^{-1} are predicted in Fig. 8, which is precisely the same range of radial velocities as is observed (when corrected for the LSR velocity of the source) across knot P.

Finally, can we distinguish between J or C-type shock excitation? The curves drawn in Fig. 8 are limited to values of α in the range 0 to $\alpha_{\rm d}$, where in each case a C-type shock speed limit is used to calculate $\alpha_{\rm d}$. The effects of using a lower H_2 dissociation speed limit are illustrated in the Appendix: here we see that because H_2 excitation is limited to lower values of α, lower radial velocities are predicted. In most of the HH 111 bow shocks, however, higher values of α are needed to produce the high radial velocities observed and particularly the highest velocities in profile line wings. A C-type excitation mechanism is therefore preferred.

4.2. Relationship of the jet and CO outflow

CO observations of the HH 111 jet reveal a two-component molecular outflow. Higher-resolution, interferometric maps show a symmetric, conical cavity of low-velocity (<10 km s^{-1}) gas that is co-axial with the HH jet (Nagar et al. 1997; Lee et al. 2000). The radius of the cavity increases from about 7″ near knot F to ∼12″ at knot P. The bulk of the molecular material in this limb-brightened cavity is situated within 30″–40″ of the VLA1 source; over most of this region the HH jet is very faint or undetected at optical wavelengths. This region presumably represents the dense core that still obscures the central outflow source. However, between HH knots F and P a fainter spur is observed which may represent material swept up by the relatively expansive bow shock P, which is of course seen at optical and near-IR wavelengths (Reipurth et al. 1997b; Coppin et al. 1998).

Sensitive, single-dish (sub)mm maps reveal, on the other hand, a chain of warm, high-velocity bullets that lie along the jet axis (Cernicharo & Reipurth 1996; Hatchell et al. 1999). Six compact bullets have been discovered, the first located a few arcseconds ahead of knot P, with the rest randomly situated further downwind. The radial LSR velocities of the bullets are between -20 km s^{-1} and -80 km s^{-1}, this velocity range is similar to the radial velocities measured for the H_2 bow shocks observed nearer the source. It seems likely that the bullets and HH jet are closely related. The bullet masses typically measure 10^{-3} $M_\odot$. Such high masses can only be explained if the bullets represent either discrete clumps ejected from the central engine (Cernicharo & Reipurth 1996) or jet material swept up along much of the path length travelled by each bullet (Hatchell et al. 1999).

If the molecular bullets do represent swept-up ambient gas, then it is likely that they are swept up by molecular shocks similar to those observed in H_2 throughout the flow. An estimate of the mass of hot H_2 associated with each HH bow shock can be made from the integrated H_2 flux (e.g. Davis et al. 2000): for a *typical* integrated H_2 1-0S(1) flux of 2.0×10^{-17} W m^{-2} for HH 111 (Gredel & Reipurth 1993), then we calculate a mass for the hot (radiating) H_2 associated with each bow, $M_{\rm H2}$, of roughly 2×10^{-7} $M_\odot$. This compares to a typical bullet mass, $M_{\rm bull} \sim 10^{-3}$ $M_\odot$ (Hatchell et al. 1999). However, the former represents only the mass of gas in the post-shock cooling zone. H_2 cooling times of the order of a few years have been inferred from observations of this and other H_2 flows (Coppin et al. 1998; Micono et al. 1998; Chrysostomou et al. 2000). The mass of each CO bullet is derived from observations of much colder gas that has been accumulated over a much longer time scale (possibly a large fraction of the dynamical age of the entire outflow). Consequently we must compare the mass accumulation rates from the two sets of observations. In other words, the rate at which H_2 passes through a molecular bow and cools should be comparable to the mass accumulation rate in the CO bullets. We can write this equality in terms of the H_2 cooling distance, $d_{\rm cool}$ and the CO bullet accumulation size scale, $d_{\rm bull}$:

$$M_{\rm H2}(v_{\rm H2}/d_{\rm H2}) \sim M_{\rm bull}(v_{\rm bull}/d_{\rm bull}) \quad (6)$$

where $v_{\rm H2}$ and $v_{\rm bull}$, the velocities of the entrained gas in the H_2 bows and CO bullets, are assumed to be equal (provided cooling has little effect on the latter). The mass ratio, $M_{\rm H2}/M_{\rm bull}$, should then be comparable to $d_{\rm H2}/d_{\rm bull}$. Given that $M_{\rm H2}/M_{\rm bull} \sim 2\times10^{-4}$ and that $d_{\rm bull}$ will be roughly equal to the distance between the CO bullets ($\sim$50″ or 3.4×10^{15} m), then the inferred H_2 cooling length is very small, of the order of 10^{12} m. Indeed, this may well be an upper limit, since it is unlikely that $M_{\rm CO}$ will be overestimated; optical depth effects will have the opposite effect, so the ratio $M_{\rm H2}/M_{\rm bull}$, and the value of $d_{\rm H2}$, could be even lower (extinction affects are not likely to effect

our H_2 mass estimate since the HH objects are optically visible).

The value of d_{H2} will of course be related to the shock excitation mechanism. It is interesting to note that only J-type shocks produce such short cooling lengths (Shull & Hollenbach 1978; Smith & MacLow 1997; Chrysostomou et al. 2000); C-type shocks produce much wider cooling zones, of the order of $10^{13}-10^{14}$ m (Smith & MacLow 1997), because the frictional drag between the ions and neutrals causes the shock layer to be spread out. Even given the uncertainties associated with the H_2 and CO bullet mass estimates, which are probably only accurate to within a factor of 10, this crude analysis does seem to support J-type shock excitation, in contrast with the C-type H_2 excitation needed to explain the high radial velocities discussed in Sect. 4.1. Although not concrete, these conflicting results do therefore point to possible difficulties with the swept-up gas model as an explanation for the observed molecular clumps. A more in-depth examination of the excitation along this jet (and in a number of other flows) will be presented in a future paper (Tedds et al. 2002).

5. Conclusions

A radial-velocity map, in H_2 1-0S(1) emission, comprising echelle spectra taken at 10 adjacent, parallel slit locations across HH 111 is presented. The blue-shifted lobe of the flow, between knot P and the source, is observed. In this region we see a transition from single-peaked, intermediate-velocity profiles in Knot P to two-component profiles between (and including) knots L and H. The same low and high-velocity H_2 components are detected towards the bright HH knot F, where we also see the greatest velocity dispersion.

We interpret the H_2 line profiles with a simple, geometrical bow shock model. Even though the model is rather basic and only 2-dimensional, we are able to explain the radial velocities quite accurately and constrain some flow parameters: we find that the two velocity components (the *LVC* and *HVC*) associated with the HH bows near to the source derive from hot, post-shock gas in the extended wings of each bow. Towards knot P, the single-peaked, intermediate-velocity profiles are accounted for if the H_2 is excited only near the head of the bow shock. In all cases, a high, pre-shock velocity, of the order of 200–250 km s^{-1}, is predicted, since the bow shocks themselves are known to be moving away from the source at about 300 km s^{-1}. The model also accounts for the fact that the *LVC* extends just ahead of the *HVC*, particularly in knot L, though also in knots H and F.

The high H_2 velocities recorded throughout the observed jet section tend to support C-type shock excitation, although J-shocks cannot be ruled out entirely.

Acknowledgements. The *UKIRT* is operated by the Joint Astronomy Centre on behalf of the UK. Particle Physics and Astronomy Research Council. We thank the Telescope System Specialist, Olga Kuhn, for helping us obtain these data so close to the holiday season. We also thanks Bo Reipurth for his comments and thorough review of this article.

Appendix: Results from the geometrical bow model

Here (Fig. A.1) we plot radial velocities predicted by the simple analytical model presented in Sect. 4.1. The model is not dependent on a pre-defined bow shock shape. Instead, it relies on the fact that, regardless of whether the bow is conical, parabolic, or hemispherical, a range of shock angles, α, will be present (α is the angle between a tangent at a given point on the shock surface and the bow axis of symmetry, which is assumed to be the same as the flow axis and axis of propagation of the bow shock). The range of velocities that one can expect to observe from the radiating, post-shock molecular gas is then limited by the velocity difference between the pre-shock gas and the bow shock. The pre-shock gas may be (i) stationary, ambient material if the bow is the leading working surface of a jet, (ii) jet material that is moving at almost the same speed as the bow if the bow represents an internal working surface along the jet axis, or (iii) slow-moving, cocoon gas that surrounds the jet beam assuming that the jet is travelling down a "swept-out" cavity. In Sect. 4.1 we assume that the H_2 emission in HH 111 is excited in only the bow shock wings and therefore describe the data in terms of case (ii). In reality, a combination of (ii) and (iii) is more likely to be the case.

The model does not consider the minimum velocities, pre-shock density and/or angle α for which observable H_2 emission will be produced. Nor do we consider the effects inhomogeneities in the preshock medium or asymmetries in the bow shock shape will have on the velocities observed. It does, nevertheless, predict the range of radial velocities one can expect to observe from the near and far sides of a bow, the main limitation being the dissociation of H_2 near the bow head for large values of α.

In Fig. A.1 we plot the radial velocity component of the post shock velocity vector that one would observe (along the line of sight) for different values of the bow and pre-shock gas velocities ($v_{\rm bow}$ and $v_{\rm coc}$ respectively) and for different viewing angles (ψ is the angle between the jet axis and the line of sight). The near and far sides of the bow are dealt with separately; two graphs are presented for each set of input parameters. In all but one case (plot V) we adopt a high value for the dissociation speed limit, $v_{\rm d}$, appropriate to a C-type shock, since this permits H_2 excitation closer to the head of the bow and so produces higher velocities. Actual observed radial velocities may be limited to lower values of α (shorter curves), as one can see by comparing the curves in plots III and V.

Finally, we also assume that emission after H_2 recombination in the post-shock cooling layer is negligeable.

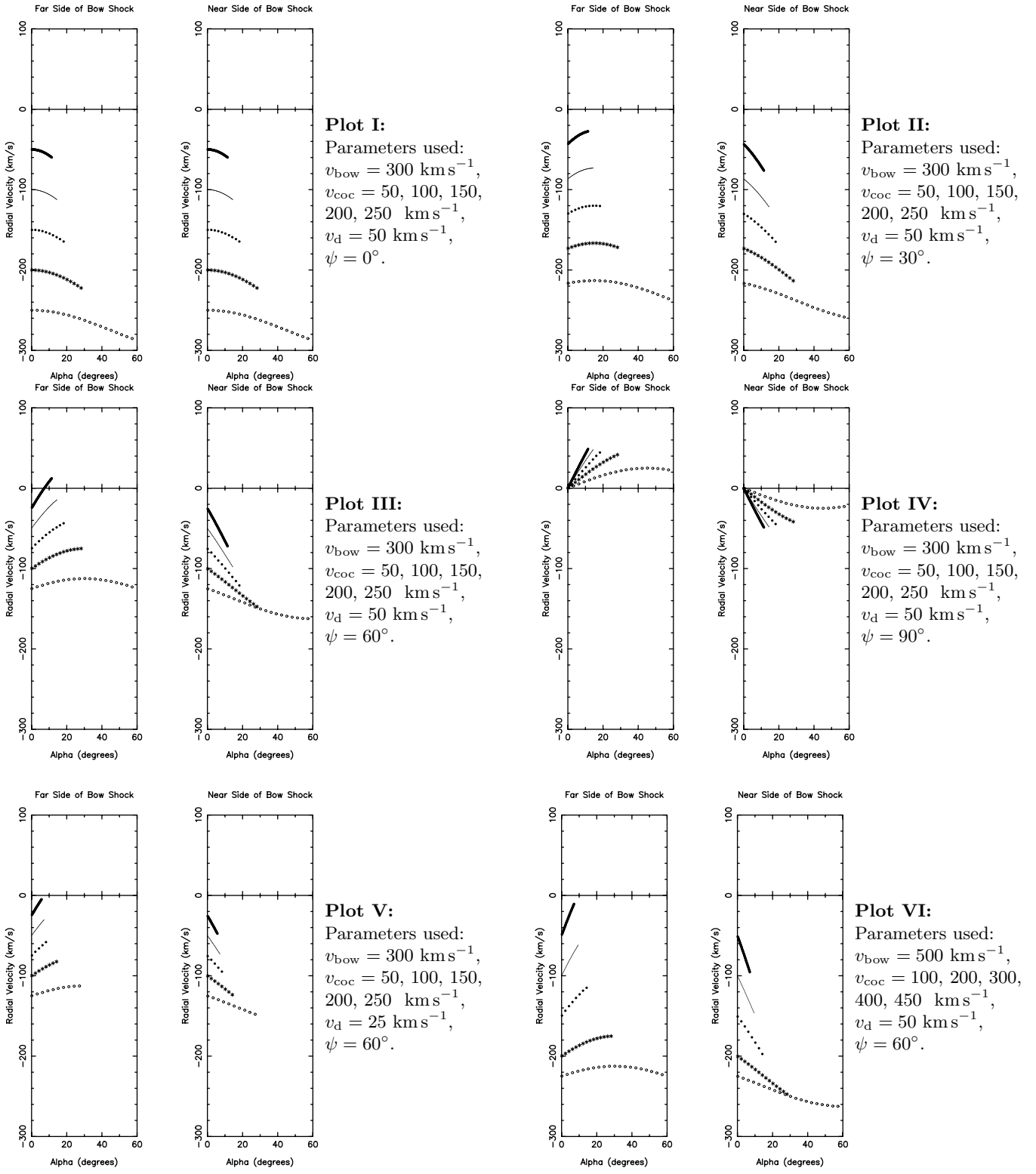

Fig. A.1. Plots of the range of radial (line-of-sight) velocities one would observe from the near and far sides of a curved shock surface (a bow shock). The maximum and minimum velocities given by each curve represent the maximum and minimum velocities one would see in the wings of an observed H_2 line profile. Each curve is limited by the maximum value of α, $\alpha_{\rm d}$ (see Eq. (5)). With the exception of Plot IV, all bows are blue-shifted; all are moving towards the observer ($\psi < 90°$). Five curves are plotted in each graph for the five values of $v_{\rm coc}$ listed; from the lowest to highest velocities given, the curves are drawn as thick line, thin line, dots, stars and circles.

References

Bragg, S. L., Smith, W. H., & Brault, J. W. 1982, ApJ, 263, 999

Cernicharo, J., & Reipurth, B. 1996, ApJ, 460, L57

Chrysostomou, A., Hobson, J., Smith, M. D., Davis, C. J., & Berndsen, A. 2000, MNRAS, 314, 229

Coppin, K. E. K., Davis, C. J., & Micono, M. 1998, MNRAS, 301, L10

Davis, C. J., Berndsen, A., Smith, M. D., Chrysostomou, A., & Hobson, J. 2000, MNRAS, 314, 241

Davis, C. J., Eislöffel, J., & Smith, M. D. 1996, ApJ, 463, 246

Davis, C. J., Mundt, R., & Eislöffel, J. 1994, ApJ, 437, L55

Davis, C. J., Ray, T. P., Desroches, L., & Aspin, C. 2001, MNRAS, 326, 524

Davis, C. J., & Smith, M. D. 1996, A&A, 309, 929

Downes, T. P., & Ray, T. P. 1999, A&A, 345, 977

Draine, B. T., Roberge, W. G., & Dalgarno, A. 1983, ApJ, 264, 485

Draine, B. T., & McKee, C. F. 1993, ARA&A, 31, 373

Gredel, R., & Reipurth, B. 1993, ApJ, 407, L29

Hartigan, P., Raymond, J. C., & Hartmann, L. 1987, ApJ, 316, 323

Hatchell, J., Fuller, G. A., & Ladd, E. 1999, A&A, 346, 584

Kwan, J. 1977, ApJ, 216, 713

Lee, C. F., Mundy, L. G., Reipurth, B., Ostriker, E. C., & Stone, J. M. 2000, ApJ, 542, 925

Micono, M., Davis, C. J., Ray, T. P., Eislöffel, J., & Shetrone, M. D. 1998, ApJ, 494, L227

Nagar, N. M., Vogel, S. N., Stone, J. M., & Ostriker, E. C. 1997, ApJ, 482, L195

Olivia, E., & Origlia, L. 1992, A&A 254, 466

Raga, A. C., Cantó, J., Binette, L., & Calvet, N. 1990, ApJ, 364, 601

Raga, A. C., Taylor, S. D., Cabrit, S., & Biro, S. 1995, A&A, 296, 833

Reipurth, B., Bally, J., & Devine, D. 1997a, AJ, 114, 2708

Reipurth, B., Hartigan, P., Heathcote, S., Morse, J. A., & Bally, J. 1997b, AJ, 114, 757

Reipurth, B., Raga, A. C., & Heathcote, S. 1992, ApJ, 392, 145

Reipurth, B., Yu, K. C., Rodríguez, L. F., Heathcote, S., & Bally, J. 1999, A&A, 352, L83

Shull, J. M., & Hollenbach, D. J. 1978, 220, 525

Smith, M. D. 1994, MNRAS, 266, 238

Smith, M. D., & Brand, P. W. J. L. 1990, MNRAS, 242, 495

Smith, M. D., & MacLow, M. M. 1997, A&A, 326, 801

Stapelfeldt, K. R., & Scoville, N. Z. 1993, ApJ, 408, 239

Tedds, J. A., Brand, P. W. J. L., & Burton, M. G. 1999, MNRAS, 307, 337

Tedds, J. A., Fernandes, A., Smith, M. D., & Davis, C. J. 2002, in preparation

Yu, K. C., Billawala, Y., Smith, M. D., Bally, J., & Butner, H. M. 2000, AJ, 120, 1974

Völker, R., Smith, M. D., Suttner, G., & Yorke, H. W. 1999, A&A, 343, 953